TUDelft

Delft University of Technology

Climate change has increased global evaporative demand except in South Asia

Karimzadeh, Saeed; Ahmadi, Arman; Baldocchi, Dennis; Fisher, Joshua B.

Important note
To cite this publication, please use the final published version (if applicable).
Please check the document version above.

Article

Climate change has increased global evaporative demand except in South Asia

Check for updates

Saeed Karimzadeh [1,2,3] ✉, Arman Ahmadi [4] ✉, Dennis Baldocchi [4] & Joshua B. Fisher [5]

Climate change alters how strongly the atmosphere draws water from the land, yet a consistent global assessment of this evaporative demand has been lacking. Here, we analyze 45 years of climate data and global models to quantify trends in the key drivers—air temperature, humidity, radiation, wind speed, and cloud cover—that determine the atmosphere's drying power. We find that evaporative demand has increased worldwide, indicating a stronger atmospheric thirst, except in South Asia, where it has declined. There, widespread irrigation has increased soil and air moisture, enhanced cloud formation, and reduced sunlight reaching the surface, counteracting the global signal. These contrasting trends reveal how human water use can locally reshape the climate's influence on the water cycle.

Debate over the intensification of the global water cycle began in the 2000s with theoretical projections, grounded in the Clausius–Clapeyron relationship, that suggested an acceleration driven by rising temperatures, though observational evidence painted a fragmented picture[1,2]. A modest 2% increase in land precipitation masked stark regional disparities, with sharp increases at higher latitudes and declines elsewhere[1,3,4]. Precipitation systems have tended to expand over tropical oceans but contract over subtropical regions[5], and extremes are projected to become ~32 ± 8% more frequent by 2100 under a medium-emissions scenario[6]. The expanding reach of extreme droughts since the 1970s[7] hints at a shifting regime, yet high interannual variability, cloud cover reversals, and ENSO-driven fluctuations obscure definitive conclusions[1]. Is the water cycle truly accelerating, or are we witnessing transient climate variability? Resolving this fundamental question demands high-resolution, long-term datasets to disentangle anthropogenic forcing from natural oscillations.

Irrigation is a key driver of environmental change with well-documented climatic impacts[8–11] and serves as a potential adaptation strategy to mitigate crop heat and water stress[12–15]. Despite covering only ~2.5% of the global land area, intensified irrigation exerts a substantial impact on regional climate[8]. Its effects vary with spatial distribution and intensity, altering hydroclimatic conditions across local, regional, and potentially global scales[16,17].

Evapotranspiration governs the terrestrial water cycle through three distinct measures: potential evapotranspiration (PET), reference (ET$_o$), and actual (AET). PET represents the atmospheric demand for water, unconstrained by water supply (soil moisture[18]). PET is the theoretical upper bound of evapotranspiration, while ET$_o$ standardizes this flux over a well-watered reference grass[19], guiding irrigation and climate assessments. Yet, AET reveals the real hydrological balance, constrained by water supply and energy demand[20], and, therefore, AET in theory cannot exceed PET[21].

Evaporation can be measured by monitoring water loss from an outdoor pan. Meanwhile, a paradox emerges in the study of pan evaporation: despite rising global temperatures, evaporation rates from open water bodies have shown a widespread decline over the past five decades[22,23]. Observations from diverse regions—including the USA[24], China[25], Australia[22], Canada[26], and India[27]—reveal a consistent, yet regionally variable, decrease in pan evaporation. This enigmatic trend, often termed the "evaporation paradox"[1,28–30], challenges the conventional expectation that warming enhances evaporation via increased vapor pressure deficit (VPD)[28]. While some attribute this phenomenon to declining wind speeds[31,32], others point to reduced solar radiation linked to aerosol-induced dimming[2]. The complexity is further amplified by measurement inconsistencies, regional meteorological variations, and the interplay between PET and AET. For example, the long-term warming trend in South Asia has remained considerably lower than the global average—an anomaly that continues to puzzle climate scientists[33]. Emerging hypotheses point to regional factors, such as high aerosol concentrations[34], which reflect solar radiation and may exert a net cooling effect, and/or large-scale irrigation expansion, which enhances evapotranspiration and suppresses surface temperatures. However, uncertainties remain about the net climatic impact of these mechanisms, warranting further investigation into their spatial and seasonal dynamics.

Some proposed that reduced pan evaporation may paradoxically signal an increase in actual evaporation[30], reshaping our understanding of land-

[1]Department of Biological and Agricultural Engineering, University of California, Davis, CA, USA. [2]Delft Center for Systems and Control, Delft University of Technology, Delft, The Netherlands. [3]Department of Built Environment, Aalto University, Espoo, Finland. [4]Department of Environmental Science, Policy and Management, University of California, Berkeley, CA, USA. [5]Schmid College of Science and Technology, Chapman University, Orange, CA, USA.
✉e-mail: saeed.karimzadeh@aalto.fi; a.ahmadi@berkeley.edu

atmosphere interactions. Is pan evaporation a fading indicator of climate change, or does it hold the key to a more profound shift in the global water cycle? Pan evaporation captures only evaporation, omitting transpiration. Alternatively, evapotranspiration can be estimated using models based on different approaches: Thornthwaite[18] (temperature-based), Priestley–Taylor[35] (radiation-based), and Penman–Monteith[19] (combined approach). Caution is needed in trend analyses, particularly with the Thornthwaite model[36]. Evaporative demand (i.e., atmospheric water demand) is the primary determinant of irrigation needs[37] via crop water requirements[19,38–40]. As the planet warms, key climate drivers, such as temperature, net radiation, wind speed, and VPD undergo changes that influence evaporative demand. Evaporative demand's sensitivity to climate variables makes it vital to understand how water usage patterns transform in a changing climate[41]. Rising global temperatures, primarily driven by anthropogenic disturbances, have been shown to increase evaporative demand[36] while rapidly reshaping the frequency and magnitude of precipitation[1], leading to potential increases in irrigation requirements in some regions and reductions in others. This variability highlights the critical need to unravel evaporative demand's spatial and temporal dynamics, as it plays a pivotal role in shaping global water cycles under changing climatic conditions.

Previous studies have documented elements of changing evaporative demand—including regional PET/ET$_o$ trends, the pan-evaporation paradox, solar dimming/brightening, wind stilling, and rising VPD—but typically in isolation, by region, without a unifying causal framework or systematic decomposition of energy drivers. Leveraging advancements in climatic reanalysis (data-driven reconstructions of past climate integrating numerical models with observational data), we employ multi-model-based evapotranspiration estimates to assess climate-driven shifts in evaporative demand, moving beyond traditional pan evaporation. Analysing 45 years of global data (1979–2023), we use the Priestley–Taylor[35] equation for PET and the FAO56 Penman–Monteith[19] equation for ET$_o$ to quantify trends while accounting for interannual trend detection limits[42]. ERA5 datasets are widely validated and often serve as a reliable source for hybrid observational-modeled data in hydrological and climate studies[43,44]. A hierarchical causal framework identifies air temperature, VPD, net radiation, and wind speed as primary drivers. To further dissect the energy driver, we evaluated net radiation through its primary constituents: net shortwave radiation, net longwave radiation, solar radiation, and its effect on surface temperature. Additionally, we investigated regional hydrological anomalies by tracing four critical variables—cloud cover, precipitation, soil moisture, and irrigation expansion—specifically as explanatory variables to provide attribution for the South Asia paradox. The results reveal that the massive expansion of irrigation across South Asia has triggered a cascading set of anomalies that decouple the region's hydroclimatic response from the globally increasing trend in evaporative demand. This framework disentangles the interplay between anthropogenic and climatic drivers of global evaporative demand.

Results and discussion

Evaporative demand arises from the combined influence of atmospheric, radiative, and land-surface processes that operate in a cascading manner (Fig. 1). At the top level, air temperature, VPD, net radiation, and wind speed form the primary determinants of evaporative demand. These variables are further regulated by secondary processes: net radiation is partitioned into net longwave and net shortwave components, the latter shaped by incoming solar radiation and modified by cloud cover. Air and surface temperature directly affect outgoing longwave fluxes, while also modulating VPD through their control on saturation vapor pressure. Land-surface processes feed back into this system: soil moisture regulates the partitioning of available energy between sensible and latent heat, influencing both surface temperature and atmospheric humidity. Precipitation replenishes soil water, while irrigated areas act as a direct anthropogenic input of moisture that alters local energy balance, cloud cover, and near-surface humidity.

Global trends of evaporative demand

The hierarchical causal framework reveals global and regional patterns of positive, negative, and nonsignificant trends ($p < 0.05$, Fig. 1). We analysed the trend of evaporative demand (annual sum of daily PET and ET$_o$) at 0.25° resolution using the Mann–Kendall test (Fig. 2). We found a statistically significant increasing trend ($p < 0.05$) in evaporative demand throughout most of the planet from 1979 to 2023 except in South Asia (i.e., India, Pakistan, Bangladesh, Nepal, Sri Lanka, Bhutan, and Maldives). Approximately 62% and 52% of terrestrial regions exhibited significant increasing trends ($p < 0.05$) in ET$_o$ and PET, respectively (Supplementary Table 1). This global increasing trend aligns with previous studies that reported an acceleration in PET and atmospheric drying power due to climate change[45–47]. In contrast, South Asia demonstrated a distinct pattern, with 72% of areas showing significant decreasing trends for ET$_o$, while 71% displayed no significant trends for PET ($p < 0.05$, Figs. 1 and 2).

The rate of decline in ET$_o$ in South Asia (-2.10 mm yr^{-2}) contrasts sharply with the rest of the global upward trend ($+0.85$ mm yr^{-2}) (Fig. 2). In 1979, the ET$_o$ in South Asia exceeded the global average by 909 mm yr^{-1} (1498 mm yr^{-1} compared to 589 mm yr^{-1}). By 2023, this disparity had narrowed substantially to 753 mm yr^{-1}, marking a 17% reduction (156 mm yr^{-1}).

Similarly, PET in South Asia surpassed the global average by 624 mm yr^{-1} in 1979 (1048 mm yr^{-1} vs. 424 mm yr^{-1}), with the gap reducing to 585 mm yr^{-1} by 2023, reflecting a 6% decrease (39 mm yr^{-1}) over the same period. A similar decline in the evaporative demand pattern in South Asia was reported previously[36]. Also, this decreasing trend was observed with the pan evaporation dataset in India[23,27] and Thailand[23,48], with a shorter analysis period.

Climatic drivers of evaporative demand

Evaporative demand is primarily driven by four interrelated meteorological variables: air temperature, solar radiation, wind speed, and VPD (Fig. 1). Global air temperature increased significantly at $+0.016$ °C yr^{-1} ($p < 0.05$), with over 80% of land areas pointing to widespread global warming (Fig. 3a and Supplementary Table 1). Warmer air has a greater capacity to hold water, leading to increased VPD when vapor pressure remains constant, thereby enhancing the atmosphere's moisture extraction capability[49]. Notably, 60% of the global terrestrial area, once South Asia is excluded, exhibited a significant increasing trend in VPD ($p < 0.05$). In contrast, South Asia demonstrated a contrasting pattern, with 80% of its areas showing a significant decline in VPD ($p < 0.05$, Fig. 3b). In other words, South Asia is becoming more humid in a warming climate, pointing to growing atmospheric water content. Human activity directly impacts water vapor concentration through irrigation[50,51].

Furthermore, South Asia exhibited anomalies in wind speed, with 71% of the region showing a significant decreasing trend ($p < 0.05$), in contrast to the predominantly stable or increasing trends observed across 95% of global land areas outside South Asia (Fig. 3d). Wind speed is a key driver of pan evaporation in India, particularly during the monsoon (Jun–Sep) and post-monsoon (Oct–Dec) seasons[27]. The finding for VPD and wind speed agrees with literature[52]. Fifty-seven percent of the global land areas (excluding South Asia) and 63% of South Asia exhibited nonsignificant trends in net radiation ($p < 0.05$, Figs. 1 and 3c). Notably, 31% of South Asia showed significant decreases in net radiation ($p < 0.05$), contrasting with 33% of the global land areas (excluding South Asia) experiencing significant increases ($p < 0.05$, Fig. 1).

Approaches to assessing evaporative demand vary in their complexity. While the ET$_o$ method accounts for aerodynamic components, such as VPD and wind speed, it simplifies the land surface by assuming a hypothetical reference crop—a grass with a height of 0.12 m, a surface resistance of 70 s m^{-1} (stomatal resistance to vapor flux), and an albedo (reflectance) of 0.23[19]. In contrast, PET emphasizes the energy balance, incorporating actual net radiation as the dominant driver of evaporative demand. Given the substantial role of energy inputs—particularly solar radiation[53]—in governing evapotranspiration, the analysis focused on net longwave and
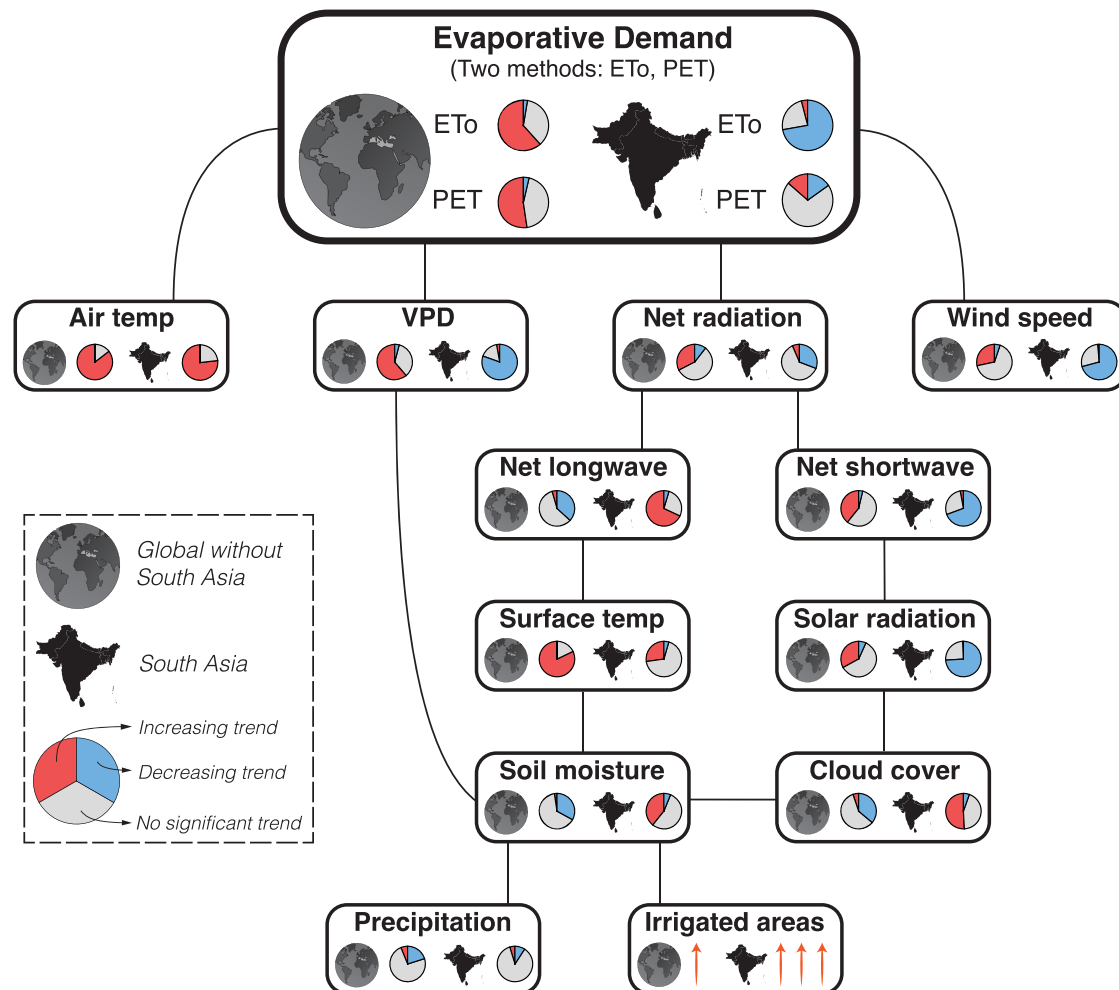
Fig. 1 | Hierarchical causal schematic representation of the variables influencing evaporative demand and their associated trends on a global scale and in South Asia. The flowchart illustrates interactions among key drivers, and the pie charts show the proportion of areas with significantly increasing, decreasing, or no trends (at $\alpha = 0.05$), highlighting regional differences and variable interconnections shaping evaporative demand.

shortwave radiation, solar radiation, and surface temperature to identify the primary drivers of observed trends (Supplementary Fig. 1).

Radiation as the source of energy
The two components of net radiation—shortwave and longwave radiation—exhibited contrasting global trends. In South Asia, these trends deviated significantly ($p < 0.05$) from the global patterns. Remarkably, net longwave radiation, defined as incoming minus outgoing longwave radiation, displayed predominantly positive trends across South Asia (Fig. 4b), with 68% of the region experiencing a significant reduction in longwave energy flux to the atmosphere ($p < 0.05$). Conversely, net shortwave radiation (Fig. 4c) showed significant negative trends ($p < 0.05$), with 69% of the area declining.

Further analysis revealed that this negative trend in net shortwave radiation in South Asia corresponded with a similar decrease in incoming solar radiation, observed in 74% of the region and characterized by a steep decline of $-0.012 \, \text{MJ} \, \text{m}^{-2} \, \text{yr}^{-2}$ ($p < 0.05$), the most pronounced reduction among all radiation components. This decline was primarily attributed to a substantial increase in cloud cover, with 51% of the area showing significant upward trends in cloudiness ($p < 0.05$, Fig. 5c).

The reduction in incoming solar radiation also impacted surface temperature trends in South Asia, which, unlike the rest of the world, showed no significant upward trajectory ($p < 0.05$). Surface temperatures remained relatively stable, from 21.7 °C in 1979 to 21.6 °C in 2023. In contrast, global surface temperatures outside South Asia increased from

5.4 °C in 1979 to 6.2 °C in 2023, reflecting a significant warming trend of $+0.015 \, \text{°C} \, \text{yr}^{-2}$ ($p < 0.05$).

Irrigation expansion's cascading effects
The findings point to a statistically significant increase ($p < 0.05$) in cloud cover in South Asia from 1979 to 2023, while most terrestrial regions of the world have experienced a substantial decline in cloud cover (Fig. 5a). This increase in cloud cover aligns with the increasing trend in atmospheric humidity (Figs. 5b and 3b). Higher atmospheric moisture has resulted in accelerated cloud formation and reduced incoming radiation in a positive feedback cycle. While some studies attribute land humidity trends primarily to oceanic moisture advection[54], others underscore the importance of terrestrial sources[55]. We identified intensified irrigation as the primary driver of increasing atmospheric humidity and explored the underlying mechanisms contributing to this phenomenon.

The large-scale irrigation expansion (Fig. 5e) has substantially impacted the climate. This interpretation is consistent with literature that attribute increases in near-surface humidity over India[56] primarily to irrigation expansion. Previous studies indicated that South Asia (India in particular) has undergone considerable unsustainable irrigation[12] expansion, usually at the cost of groundwater overdraft[49], where irrigation application can reach an annual average rate of more than 1800 mm yr^{-1}. Irrigation reduced the sensible heat flux due to an increase in latent heat flux, thereby lowering the surface temperature[14,57]. Irrigation expansion (82% unsustainable[58]) in South Asia (Fig. 5f) was reflected in soil moisture
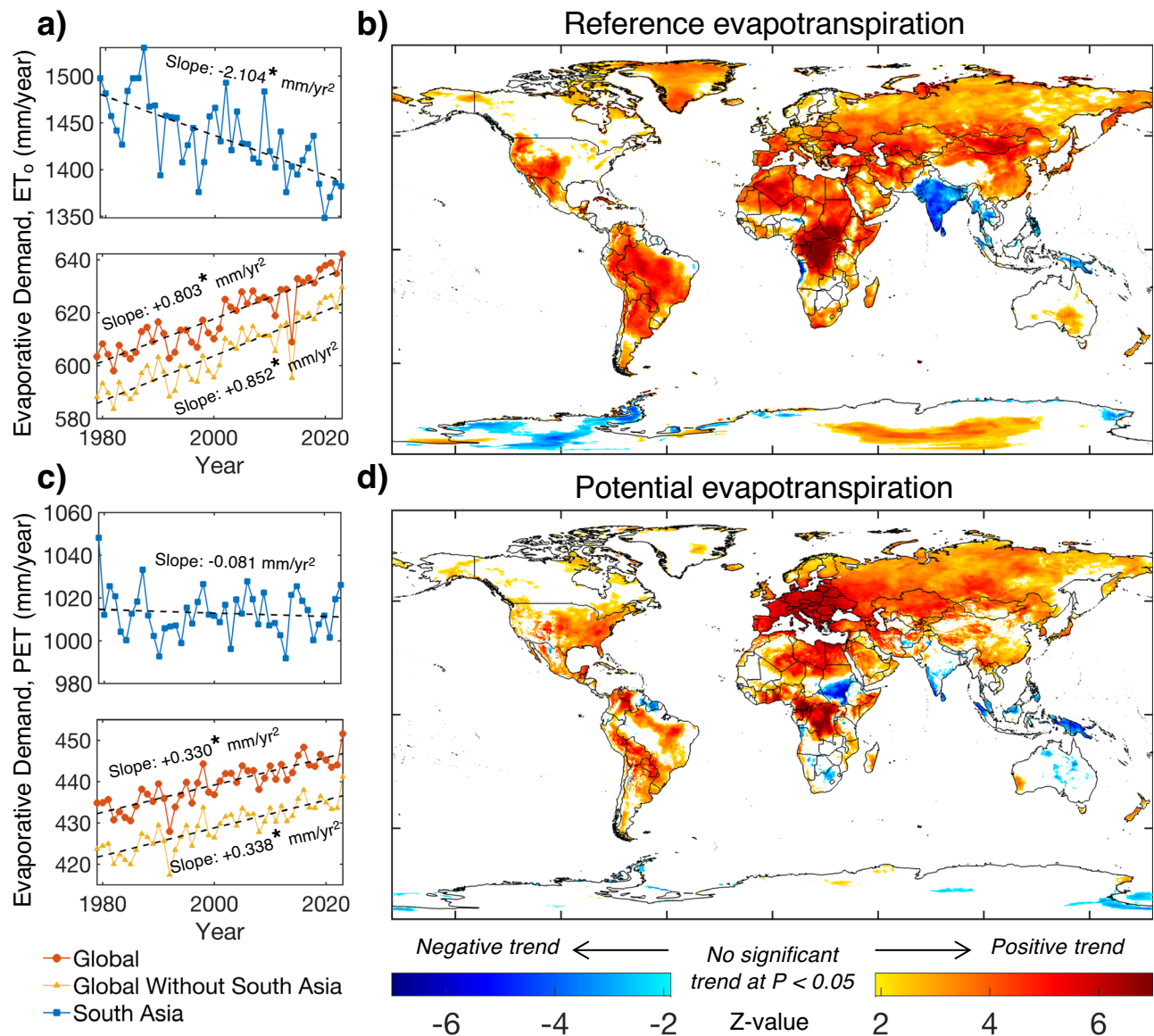
Fig. 2 | Trends in reference evapotranspiration (ET$_o$) and potential evapotranspiration (PET) show significant increases globally, except in South Asia. **a, c** Show time series of global, global excluding South Asia, and South Asia trends in annual ET$_o$ and PET (mm yr^{-1}). **b, d** Spatial patterns of significant positive (red), significant negative (blue), and nonsignificant trends in ET$_o$ and PET, respectively, as determined by the Mann–Kendall test's Z-value. Areas shown in white represent oceans, water bodies, or land regions with no significant trend. Statistically significant slope trends ($\alpha = 0.05$) are marked with an asterisk (*).

anomalies (Fig. 5d), which has contributed considerably to higher atmosphere moisture content (Fig. 5b) in a cascading manner. Notably, this rise in soil moisture cannot be attributed to natural causes, as precipitation trends in South Asia showed no significant changes, even as global average precipitation declines (Fig. 5c). Thus, interestingly, this anthropogenic irrigation expansion in South Asia caused significant negative trends in VPD ($p < 0.05$, Figs. 3b and 5b), incoming solar radiation (Fig. 4d), and have potentially contributed to wind speed (Fig. 3d), despite the global warming trend (Fig. 3a). The reduction of surface winds may be attributed to irrigation-induced surface air cooling, which enhances atmospheric column stability, thereby reducing turbulent momentum transport[59]. The patterns of shortwave radiation, cloud cover, and net radiation are consistent with previously reported cascading processes[60], where intensified irrigation in the Tarim Basin alters atmospheric moisture transport, enhancing summer snowfall in the Kunlun Shan and reducing glacier melt by lowering net radiation through increased cloud cover and surface albedo.

An alternative mechanism for such anomalies in South Asia could be the rise in vapor pressure reflects enhanced advection of oceanic moisture

from the Arabian Sea and the Bay of Bengal, which could also account for the observed increases in cloud cover and reductions in VPD. Under this mechanism, reduced incoming solar radiation and suppressed VPD would lower AET, leading to soil moisture accumulation even in the absence of precipitation changes. This stands in contrast to the irrigation hypothesis, under which irrigation expansion is expected to elevate AET and atmospheric humidity while simultaneously reducing ET$_o$. Conversely, the ocean-advection mechanism suggests that increased humidity suppresses both AET and ET$_o$, reflecting an atmospheric evaporative demand-driven pathway. Nevertheless, several studies have reported increases in AET across South Asia[61–64] making this mechanism unlikely to be the primary driver of the observed phenomenon in South Asia. Recent evidence indicates that rising AET in this region is predominantly driven by leaf area index, rather than by precipitation or atmospheric evaporative demand[64], reflecting irrigation-induced intensification of crop production and the regulatory role of vegetation in moderating atmospheric humidity deficits[65]. Taken together, the concurrence of (i) extensive irrigation expansion[58,66] with high magnitude of irrigation volume[67], (ii) prevailing moisture flux
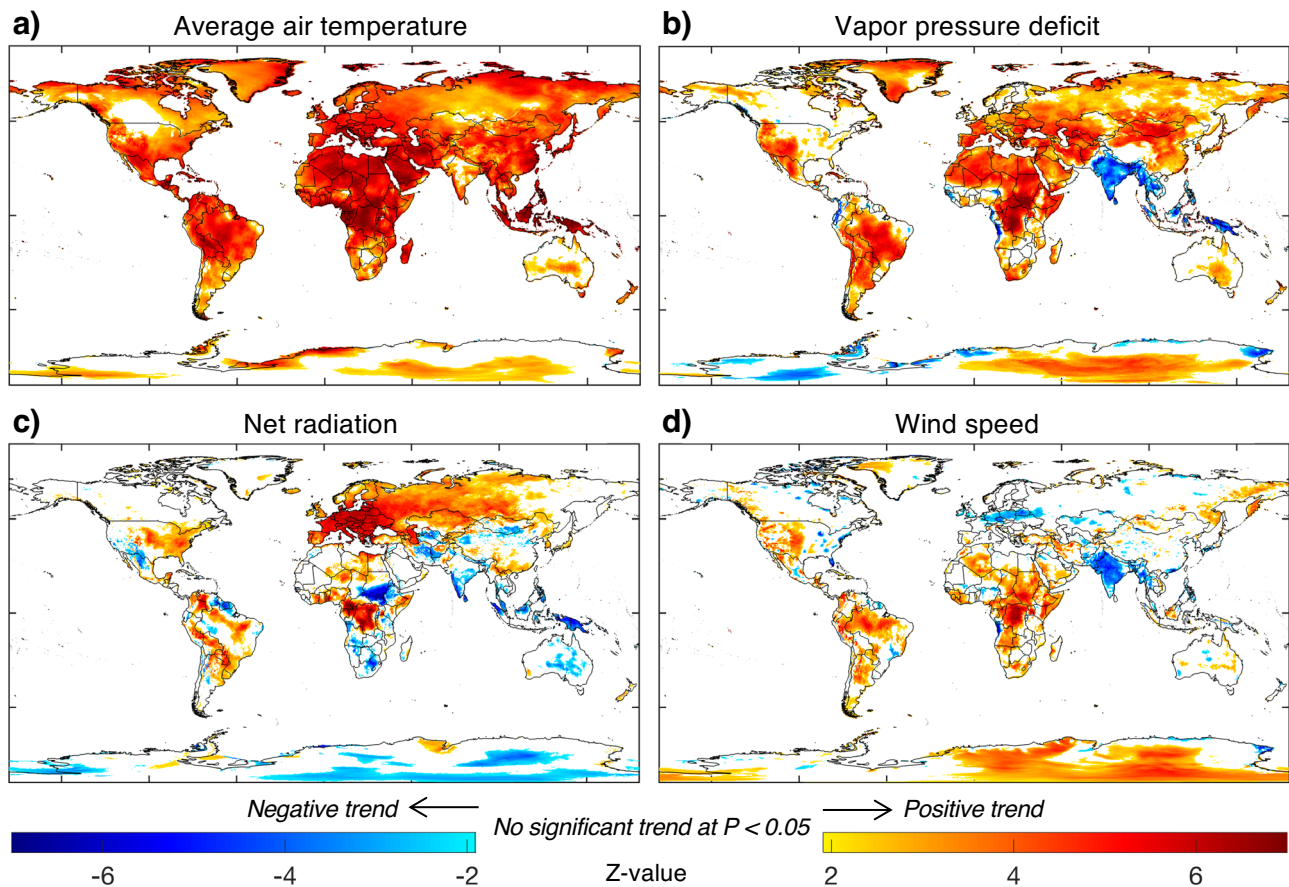
Fig. 3 | Climate variables multi-decadal trend (Z-value) from 1979 to 2023 show drivers of evaporative demand. This figure presents the spatial pattern (map) of statistically significant trends in air temperature (°C, **a**), vapor pressure deficit (kPa, **b**), net radiation (MJ m^{-2}, **c**), and wind speed (m s^{-1}, **d**)—key meteorological variables driving evaporative demand. The trends are determined using the Mann–Kendall test's Z-value. White areas indicate oceans, water bodies, or land regions with no statistically significant trend at $\alpha = 0.05$.

pathways[68], (iii) predominantly declining ocean evaporation[69], and (iv) altered near-surface wind patterns[70] provides a coherent explanation for why the humidity signal is particularly distinct in South Asia.

Although irrigation expansion has also occurred in Northeast Asia, its extent is comparatively modest relative to South Asia (Supplementary Fig. 2). The prevailing atmospheric moisture flux[68] in this region is directed predominantly toward the East China Sea and the North Pacific Ocean. Concurrently, a notable decline in ocean evaporation (-25 to -50 mm yr^{-2}) over the East China Sea is evident[69], contributing to an enhanced regional moisture deficit. When considered together, the flux direction and reduced oceanic evaporation imply that the irrigation-induced atmospheric moisture signal in Northeast Asia is substantially weaker than that observed in South Asia. This interpretation is further supported by declining near-surface wind speed trends[70], which indicate strengthened advection of atmospheric moisture along this pathway. Similarly, a marked reduction in ocean evaporation over the North Atlantic generates a substantial atmospheric moisture deficit in North America. Meanwhile, it is important to note that a comparable mechanism of irrigation-induced moisture transport has been documented in California's Central Valley[15]. Unlike the annual-scale trend observed elsewhere, this effect manifests seasonally (Jun–Aug). In this context, irrigation enhances water vapor transport that initiates atmospheric instabilities over the southwestern U.S., with soil moisture feedback and lateral water vapor convergence amplifying regional precipitation.

Heightened AET due to irrigation can increase near-surface humidity, moist static energy (the sum of the internal, potential, and latent energy content of a parcel of air), and convective available potential energy (a measure of the atmosphere's ability to support rising air, leading to cloud formation and storms) in some areas[65]. In other words, irrigation can greatly impact the climate by increasing AET, which lowers the ratio of sensible to latent heat (Bowen ratio)[49]. This human-driven atmospheric moisture can lead to greater cloud cover, triggering a positive feedback mechanism by diminishing the amount of incident shortwave radiation and net radiation[8]. Such land-atmosphere feedback suggests that human water management can counteract, at least regionally, the expected acceleration of the hydrological cycle. This highlights the dual role of irrigation as both a climate adaptation measure and a driver of climatic anomalies, raising critical questions about its sustainability under increasing water stress.

South Asia is home to nearly one-quarter of the global population and is highly vulnerable to climate change–induced agricultural productivity losses, which have negatively affected food production and prices across the region[71]. Nevertheless, food security in South Asia improved substantially—rising by ~120% between 1989 and 2020[72]—largely through the expansion of irrigation that boosted total food production. This adaptation, however, comes with trade-offs: while irrigation expansion has helped offset climate-related yield losses, the region faces growing water scarcity driven by population growth, agricultural intensification, and rapid urbanization. Climate change is intensifying floods, droughts, and cyclones, and without effective adaptation, South Asia faces projected gross domestic product losses of ~6% annually by 2050 from worsening water scarcity[73].

At a broader scale, the results illustrate that water-cycle intensification is neither spatially uniform nor temporally consistent. While some regions show clear acceleration of evaporative demand, others exhibit stabilization or decline depending on the interplay of drivers. This heterogeneity emphasizes that projections of future drought, precipitation extremes, and irrigation demand cannot rely solely on temperature trajectories, but must
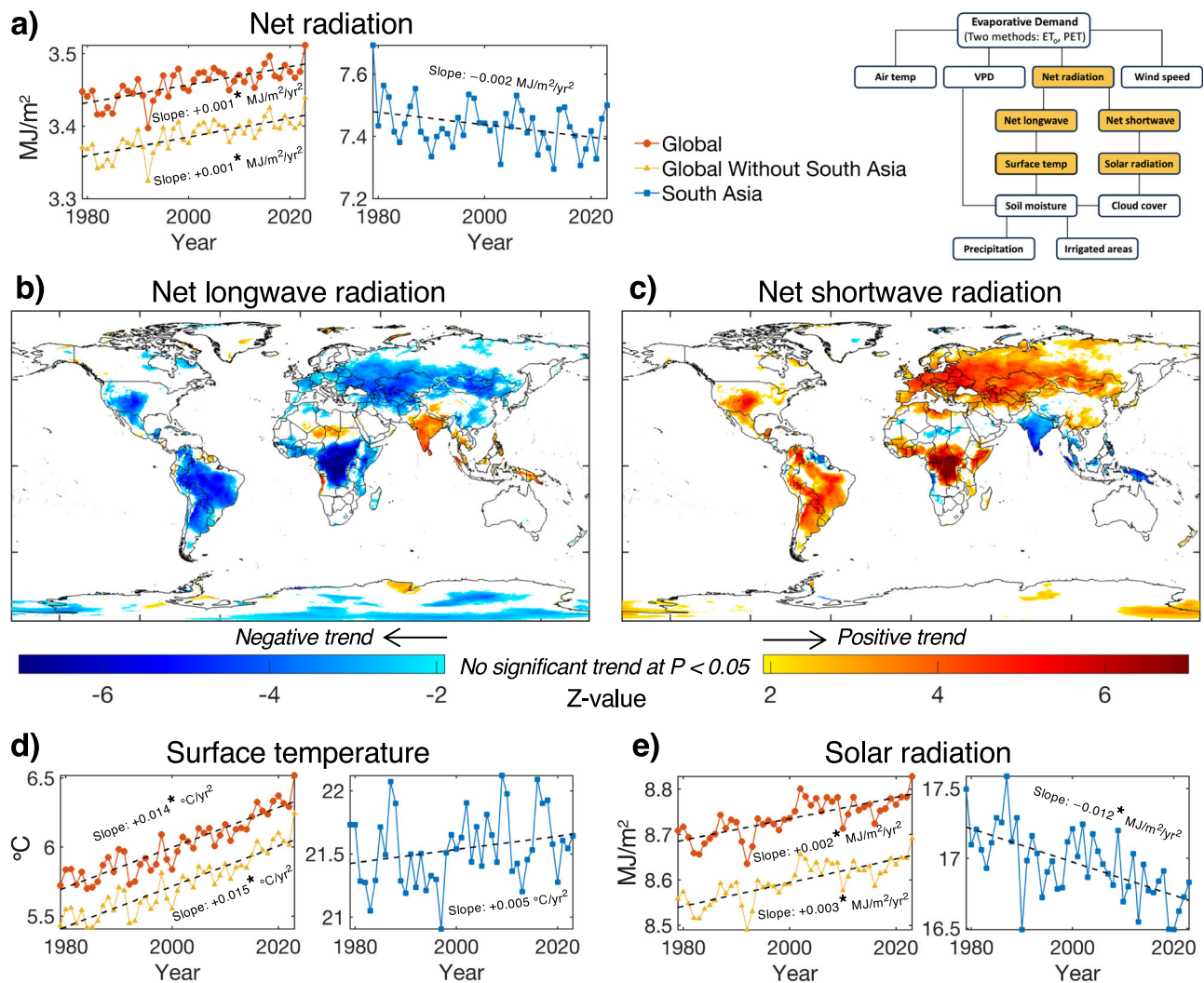
Fig. 4 | **Global increasing trends in radiation components and surface temperature, which are the primary drivers of evaporative demand, compared to anomalies in South Asia. a** Net radiation trends. **b, c** Map spatial trends (Z-value) in net longwave (incoming minus outgoing) and shortwave radiation, highlighting contrasting patterns. **d** Rising global surface temperatures. **e** Rising solar radiation globally but steep declines in South Asia. Statistically significant slope trends ($\alpha = 0.05$) are marked with an asterisk (*). The schematic links radiation components to evaporative demand drivers.

incorporate multi-variable frameworks that consider radiation, wind, humidity, and land use. The hierarchical causal framework provides one such integrative approach, revealing how atmospheric drivers, surface energy balance, and land-atmosphere mediators interact to shape regional hydroclimatic outcomes.

Conclusion

This study reveals critical insights into global evaporative demand and its climatic drivers from 1979 to 2023. We find that global evaporative demand has increased significantly ($p < 0.05$) due to climate change, with an average rise of $+0.33$ mm yr^{-2} in PET and $+0.80$ mm yr^{-2} in ET$_\mathrm{o}$. However, South Asia deviates from this global pattern, showing a unique and statistically significant decrease in ET$_\mathrm{o}$ by -2.10 mm yr^{-2} ($p < 0.05$) and no significant trend in PET. Analysing trends in 11 critical atmospheric and surface variables—air temperature, VPD, net radiation (inclusive of longwave and shortwave components), solar radiation, wind speed, surface temperature, cloud cover, precipitation, and soil moisture—within a hierarchical causal framework, reveal a statistically significant increase in cloud cover and decrease in incoming solar radiation over South Asia, in contrast to most terrestrial regions. While precipitation in South Asia showed no significant trend, soil moisture exhibited a significant increase, alongside a significant decline in VPD ($p < 0.05$). These results underscore the profound

anthropogenic influence of extensive irrigation expansion in South Asia, driving climatic anomalies in this region. This massive-scale artificial impact offers vital insights for policymakers on sustainable water resource management and food production in an era of climate change.

Methods
Data

Time-series data from 1979 to 2023 (45 years), including maximum, minimum, mean and dew point air temperatures (all temperatures measured at a height of 2 m above the surface), surface temperature (temperature of the soil in 0–7 cm), solar radiation, net shortwave radiation, net longwave radiation, precipitation, soil moisture (volume of water in soil 0–7 cm), cloud cover, and wind speed (wind speed measured at a height of 10 m above the surface), was acquired from the ERA5 Agrometeorological Climate Reanalysis by the European Centre for Medium-Range Weather forecasts at a spatial resolution of 0.1°[74,75]. The ERA5 datasets exhibit consistency with most of variables reported by AmeriFlux[76], and FLUXNET[77] (a network of eddy covariance towers that measures land-atmosphere exchanges of carbon, water, and energy[78]). Wind speed data were converted to a height of 2 m using the wind profile relationship[19]. Additionally, dew point temperature was used to estimate saturation vapor pressure[19]. For elevation data, the Global Multi-resolution Terrain Elevation Data 2010
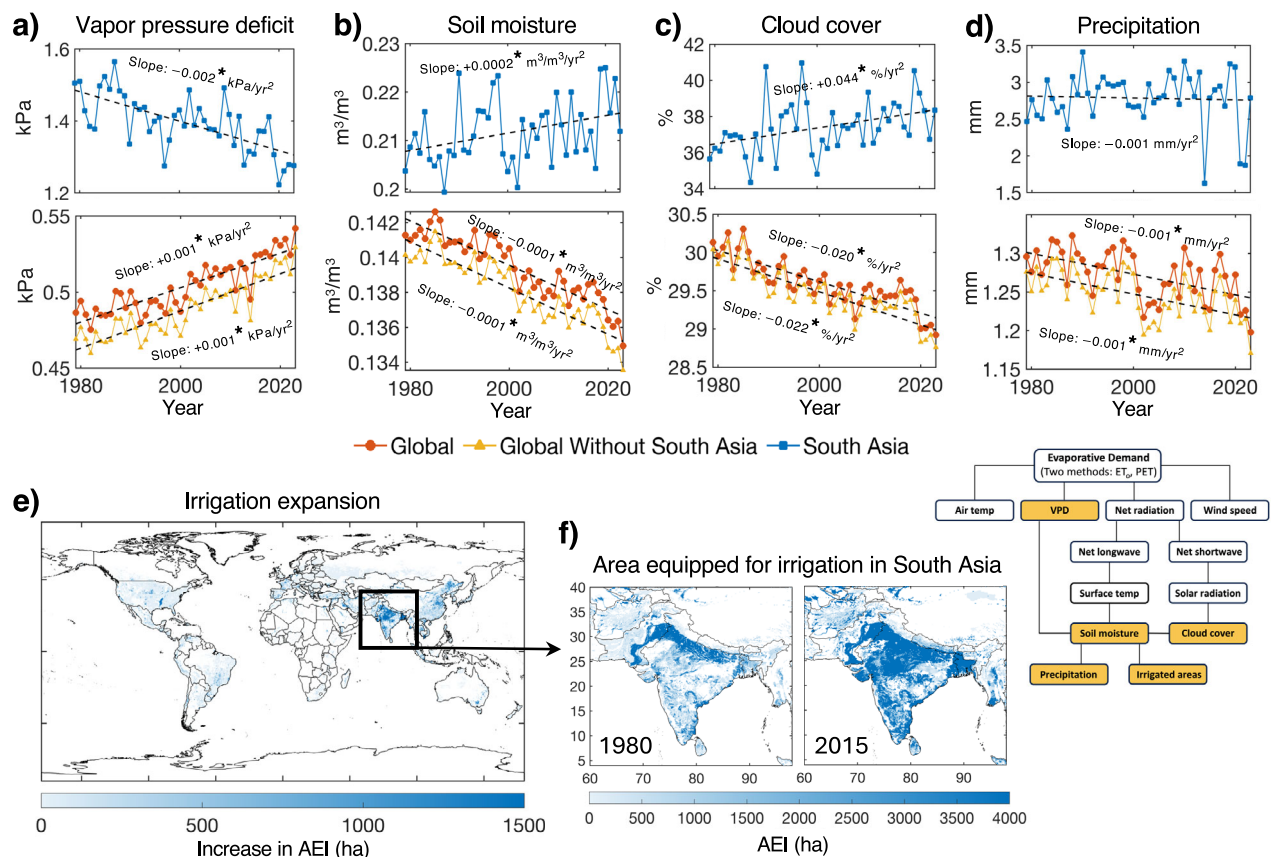
Fig. 5 | Massive irrigation expansion in South Asia disrupts global multi-decadal trends, leading to regional anomalies in key atmospheric and land surface variables. a–d Time series trends for these variables across global, global excluding South Asia, and South Asia regions. **e** The global increase in the area equipped for irrigation (AEI), with South Asia highlighted as a hotspot of irrigation expansion. **f** Historical maps of AEI in South Asia in 1980 and 2015, showing substantial increases. The orange-highlighted variables in the flowchart indicate their focus in this figure, building upon the framework detailed in Fig. 1. This analysis emphasizes the interplay between climate variables and human-driven irrigation changes in shaping global evaporative demand dynamics.

dataset[79] was utilized. The global historical area equipped for irrigation (AEI) dataset[58,66], spanning from 1900 to 2015, was obtained at a spatial resolution of 0.0833°.

Reanalysis products, such as ERA5, integrate a wide range of observational data with numerical weather prediction models through data assimilation techniques[80]. ERA5 provides a globally consistent and spatially complete estimate of atmospheric conditions at regular temporal intervals[44]. Despite their strengths, reanalysis datasets are not direct observations at all times and locations and may subject to model-related biases and uncertainties[80]. Meanwhile, ERA5 has been widely validated and can serve as a reliable proxy for observational data in the simulation and evaluation of hydrological and climatic processes[43,44,81] due to its long historical record. Ideally, comprehensive in situ measurements across all spatial and temporal scales would offer the most accurate assessment of environmental uncertainties. However, such coverage remains infeasible, especially in remote and data-scarce regions like the Sahara Desert, Amazon Basin, Australian Outback, and polar zones[82].

Reference evapotranspiration

The FAO56 Penman–Monteith equation is employed to estimate the daily ET_o[19]. The model is represented by Eq. 1:

$$ET_o = \frac{0.408\,\Delta\,(R_n - G) + \gamma\,\frac{900}{T+273}\,u_2\,(e_s - e_a)}{\Delta + \gamma\,(1 + 0.34u_2)} \quad (1)$$

ET_o is the reference evapotranspiration (mm day^{-1}), R_n is the net radiation at the reference crop surface (MJ m^{-2} day^{-1}), G is the soil heat flux

density (MJ m^{-2} day^{-1}) and is assumed to be zero for daily calculations[19], T is the average daily air temperature at 2 m height (°C), u_2 is the wind speed at 2 m height (ms^{-1}), e_s is the saturation vapor pressure (kPa), e_a is the actual vapor pressure (kPa), $e_s - e_a$ is the saturation VPD (kPa), Δ is the slope of the vapor pressure curve (kPa °C^{-1}), and γ is the psychrometric constant (kPa °C^{-1}). Detailed procedures for ET_o estimation are followed based on the FAO56 paper[19].

Slope of saturation vapor pressure curve (Δ): it quantifies the rate of change of the saturation vapor pressure with respect to average temperature:

$$\Delta = \frac{4098 * 0.6108\,exp(\frac{17.27\,\times\,T_{ave}}{T_{ave}+237.3})}{(T_{ave} + 237.3)^2} \quad (2)$$

Here, T_{ave} represents the average air temperature (°C) at a height of 2 m above the surface.

Net radiation at the reference crop surface (R_n): it is the sum of the net shortwave and net longwave radiation (R_{ns}, MJ m^{-2} day^{-1}) and the net longwave (R_{nl}, MJ m^{-2} day^{-1}):

$$R_n = R_{ns} + R_{nl} \quad (3)$$

The net shortwave radiation (R_{ns}) represents the portion of solar radiation R_s that is not reflected by the surface. The proportion of solar radiation that the surface reflects is called albedo. For the reference crop of

green grass, albedo is 0.23. Therefore, the value of R_{ns} is:

$$R_{ns} = R_s * (1 - \text{albedo}) \tag{4}$$

The net longwave radiation (R_{nl}) is incoming minus outgoing long-wave radiation. According to the Stefan–Boltzmann law, longwave energy emission is dependent on surface temperature. The net energy flux departing from the Earth's surface is also affected by cloud cover and humidity.

$$R_{nl} = \sigma \times \left(\frac{T_{max,K}^2 + T_{min,K}^2}{2} \right) * \left(0.34 - 0.14 * \sqrt{e_a} \right) * \left(0.35 - 1.35 * \frac{R_s}{R_{so}} \right) \tag{5}$$

σ represents the Stefan–Boltzmann constant (4.903×10^{-9} MJ K^{-4} m^{-2} day^{-1}), $T_{max,K}$ and $T_{min,K}$ are the maximum and minimum temperatures in Kelvin, e_a is the actual vapor pressure, R_s denotes the measured solar radiation (MJ m^{-2} day^{-1}), and R_{so} is the calculated clear-sky radiation (MJ m^{-2} day^{-1}). It is worth noting that the sign convention in Eq. 5 is opposite to that in FAO56, as we define R_{nl} as incoming minus outgoing, while FAO56 defines it oppositely. The calculation of R_{so} depends on extraterrestrial solar radiation (R_a, MJ m^{-2} day^{-1}) and elevation (elev, m).

$$R_{so} = R_a * (0.75 + 0.00002 * elev) \tag{6}$$

Extraterrestrial radiation (R_a, MJ m^{-2} day^{-1}) is radiation from sources outside Earth (primarily the Sun and other celestial bodies)

$$R_a = \frac{24(60)}{\pi} G_{sc} d_r \left[\omega_s \sin(\varphi) \sin(\delta) + \cos(\varphi) \cos(\delta) \sin(\omega_s) \right] \tag{7}$$

$$d_r = 1 + 0.033 \cos\left(\frac{2\pi}{365} J \right) \tag{8}$$

$$\delta = 0.409 \sin\left(\frac{2\pi}{365} J - 1.39 \right) \tag{9}$$

$$\omega_s = \arccos[-\tan(\varphi)\tan(\delta)] \tag{10}$$

G_{sc} refers to solar constant = 0.0820 MJ m^{-2} min^{-1}, d_r is inverse relative distance Earth-sun (factor in adjusting the incoming solar radiation to account for the elliptical orbit of the Earth), ω_s is sunset hour angle (rad), φ represents latitude (rad), δ is solar decimation (rad), J is the Julian day of the year.

Psychrometric constant (γ): It is expressed as:

$$\gamma = \frac{c_p * Pr}{\varepsilon * \lambda} \tag{11}$$

Here, c_p represents the specific heat capacity at constant pressure (MJ kg^{-1} $°C^{-1}$), with a value of 1.013×10^{-3}. λ denotes the latent heat of vaporization (MJ kg^{-1}), set at 2.45. Meanwhile, ε is the molecular weight ratio between water vapor and dry air, equating to 0.622. These values vary slightly with temperature, humidity, and pressure, but are adequate for average atmospheric conditions[19]. Atmospheric pressure (Pr, kPa) is the pressure caused by the weight of the atmosphere and varies with elevation (elev, m).

$$Pr = 101.3 * \left(\frac{293 - 0.0065 * elev}{293} \right)^{5.26} \tag{12}$$

Wind speed at 2 m (u_2): The wind speed dataset is provided at 10 m. Following Eq. 13 recommended in ref. 19, u_2 (ms^{-1}) is estimated:

$$u_2 = u_z \frac{4.87}{\ln(67.8z - 5.42)} = u_{10} \frac{4.87}{\ln(67.8 * 10 - 5.42)} \tag{13}$$

u_z is the measured wind speed at z meters above ground surface (ms^{-1}), and z is the height of measurement above ground surface ($z = 10$).

Saturation vapor pressure (e_s) and actual vapor pressure (e_a): the saturation vapor pressure is averaged from daily maximum ($e^0(T_{max})$) and minimum air temperatures ($e^0(T_{min})$), while the actual vapor pressure is based on the dewpoint temperature ($e^0(T_{dew})$).

$$e_s = \frac{e^0(T_{max}) + e^0(T_{min})}{2} \tag{14}$$

$$e^0(T_{max}) = 0.6108 \exp\left(\frac{17.27 T_{max}}{T_{max} + 237.2} \right) \tag{15}$$

$$e^0(T_{min}) = 0.6108 \exp\left(\frac{17.27 T_{min}}{T_{min} + 237.2} \right) \tag{16}$$

$$e_a = e^0(T_{dew}) = 0.6108 \exp\left(\frac{17.27 T_{dew}}{T_{dew} + 237.2} \right) \tag{17}$$

Potential evapotranspiration

The Priestley–Taylor model[35] is a widely used framework for estimating potential PET emphasizing surface energy balance and simplifying aerodynamic complexities. The Priestley–Taylor model is provided in Eq. 18:

$$PET = \alpha \frac{\Delta}{\Delta + \gamma} \left(\frac{R_n - G}{\lambda} \right) \tag{18}$$

It uses net radiation (R_n, MJ m^{-2} day^{-1}, Eq. 5) with net shortwave and longwave components derived directly from ERA5 radiation variables, and ground heat flux (G, MJ m^{-2} day^{-1}) as primary drivers, with the dimensionless coefficient α (typically 1.26) accounting for non-radiative processes under well-watered conditions. By integrating the thermodynamic parameters of the vapor pressure curve slope (Δ, kPa $°C^{-1}$) the psychrometric constant (γ, kPa $°C^{-1}$) and the latent heat of vaporization (λ, 2.45 MJ kg^{-1}), the model captures key drivers of PET and essential for hydrological and climate studies while requiring minimal meteorological inputs.

Mann–Kendall trend analysis

To examine the trends in the variables, we applied the Mann–Kendall (MK) test[83,84]. The MK trend test evaluates significance using ranks, assessing whether the statistic S of the time series falls within the confidence interval of the null hypothesis at a specified significance level (α)[85]. This nonparametric test is applicable to both Gaussian and non-Gaussian data, making it distribution-free. Therefore, it operates effectively across all distributions without requiring assumptions of normality[53]. The null hypothesis of the MK test assumes no monotonic trend in the data, with the alternative hypothesis indicates the presence of such a trend. In our analysis, a significance level of $\alpha = 0.05$ determines whether to reject the null hypothesis based on the P-value obtained from each test. In this study, the MK test score undergoes Z-score normalization. The sign of Z indicates the trend direction, while $Z > 1.96$ denotes a significant positive trend (increasing values over time), while $Z < -1.96$ denotes a significant negative trend (decreasing values over time). The calculated Z-values supporting this study are deposited online (see ref. 86).

Data availability

The digital elevation model of the terrain was obtained from the U.S. Geological Survey[79] (USGS) [https://doi.org/10.3133/ofr20111073]. The

global map of areas equipped with irrigation was retrieved from Siebert et al.[66] and Mehta et al.[58], [https://doi.org/10.5194/hess-19-1521-2015; https://doi.org/10.1038/s44221-024-00206-9]. Climate variables used in the hierarchical causal schematic (Fig. 1) are publicly available from the Copernicus Climate Data Store [https://cds.climate.copernicus.eu/datasets; last accessed on 22 October 2025] and were subsequently processed as described in the "Methods". The Z-values from all trend analyses are deposited[86] in Zenodo (https://doi.org/10.5281/zenodo.17098484).

Code availability
All maps and figures were generated in MATLAB R2024b. The results of the analytical codes are publicly archived in Zenodo (https://doi.org/10.5281/zenodo.17098484).

References
1. Huntington, T. G. Evidence for intensification of the global water cycle: review and synthesis. *J. Hydrol.* **319**, 83–95 (2006).
2. Ohmura, A. & Wild, M. Is the hydrological cycle accelerating? *Science* **298**, 1345–1346 (2002).
3. Dai, A., Fung, I. Y. & Del Genio, A. D. Surface observed global land precipitation variations during 1900–88. *J. Clim.* **10**, 2943–2962 (1997).
4. Hulme, M., Osborn, T. J. & Johns, T. C. Precipitation sensitivity to global warming: Comparison of observations with HadCM2 simulations. *Geophys. Res. Lett.* **25**, 3379–3382 (1998).
5. Zhang, Y. & Wang, K. Global precipitation system scale increased from 2001 to 2020. *J. Hydrol.* **616**, 128768 (2023).
6. Thackeray, C. W., Hall, A., Norris, J. & Chen, D. Constraining the increased frequency of global precipitation extremes under warming. *Nat. Clim. Change* **12**, 441–448 (2022).
7. Dai, A., Trenberth, K. E. & Qian, T. A global dataset of Palmer drought severity index for 1870–2002: relationship with soil moisture and effects of surface warming. *J. Hydrometeorol.* **5**, 1117–1130 (2004).
8. McDermid, S. et al. Irrigation in the Earth system. *Nat. Rev. Earth Environ.* **4**, 435–453 (2023).
9. Mahmood, R. et al. Land cover changes and their biogeophysical effects on climate. *Int. J. Climatol.* **34**, 929–953 (2014).
10. Lobell, D. B., Bonfils, C. J., Kueppers, L. M. & Snyder, M. A. Irrigation cooling effect on temperature and heat index extremes. *Geophys. Res. Lett.* **35**, 2008GL034145 (2008).
11. Lobell, D. B. & Bonfils, C. The effect of irrigation on regional temperatures: a spatial and temporal analysis of trends in California, 1934–2002. *J. Clim.* **21**, 2063–2071 (2008).
12. Rosa, L. Adapting agriculture to climate change via sustainable irrigation: biophysical potentials and feedbacks. *Environ. Res. Lett.* **17**, 063008 (2022).
13. Rosa, L. et al. Potential for sustainable irrigation expansion in a 3 °C warmer climate. *Proc. Natl. Acad. Sci. USA* **117**, 29526–29534 (2020).
14. Wang, W. et al. The climatic effects of irrigation over the middle and lower reaches of the Yangtze River, China. *Agric. For. Meteorol.* **308–309**, 108550 (2021).
15. Lo, M. & Famiglietti, J. S. Irrigation in California's central valley strengthens the southwestern U.S. water cycle. *Geophys. Res. Lett.* **40**, 301–306 (2013).
16. Barnston, A. G. & Schickedanz, P. T. The effect of irrigation on warm season precipitation in the Southern Great Plains. *J. Clim. Appl. Meteorol.* **23**, 865–888 (1984).
17. Greve, P. et al. Observational evidence of increased afternoon rainfall downwind of irrigated areas. *Nat. Commun.* **16**, 3415 (2025).
18. Thornthwaite, C. W. An approach toward a rational classification of climate. *Geogr. Rev.* **38**, 55 (1948).
19. Rick, G. A. Crop evapotranspiration: *Guidelines for Computing Crop Water Requirements* (Food and Agriculture Organization of the United Nations, 1998).
20. Jung, M. et al. Recent decline in the global land evapotranspiration trend due to limited moisture supply. *Nature* **467**, 951–954 (2010).
21. Fisher, J. B., Whittaker, R. J. & Malhi, Y. ET come home: potential evapotranspiration in geographical ecology. *Glob. Ecol. Biogeogr.* **20**, 1–18 (2011).
22. Roderick, M. L. & Farquhar, G. D. The cause of decreased pan evaporation over the past 50 years. *Science* **298**, 1410–1411 (2002).
23. Roderick, M. L., Hobbins, M. T. & Farquhar, G. D. Pan evaporation trends and the terrestrial water balance. II. Energy balance and interpretation. *Geogr. Compass* **3**, 761–780 (2009).
24. Peterson, T. C., Golubev, V. S. & Groisman, P. Ya. Evaporation losing its strength. *Nature* **377**, 687–688 (1995).
25. Liu, B., Xu, M., Henderson, M. & Gong, W. A spatial analysis of pan evaporation trends in China, 1955–2000. *J. Geophys. Res.* **109**, 2004JD004511 (2004).
26. Burn, D. H. & Hesch, N. M. Trends in evaporation for the Canadian Prairies. *J. Hydrol.* **336**, 61–73 (2007).
27. Chattopadhyay, N. & Hulme, M. Evaporation and potential evapotranspiration in India under conditions of recent and future climate change. *Agric. For. Meteorol.* **87**, 55–73 (1997).
28. Fu, G., Charles, S. P. & Yu, J. A critical overview of pan evaporation trends over the last 50 years. *Clim. Change* **97**, 193–214 (2009).
29. Xing, W. et al. Periodic fluctuation of reference evapotranspiration during the past five decades: does evaporation Paradox really exist in China? *Sci. Rep.* **6**, 39503 (2016).
30. Brutsaert, W. & Parlange, M. B. Hydrologic cycle explains the evaporation paradox. *Nature* **396**, 30–30 (1998).
31. Rayner, D. P. Wind run changes: the dominant factor affecting pan evaporation trends in Australia. *J. Clim.* **20**, 3379–3394 (2007).
32. Roderick, M. L., Rotstayn, L. D., Farquhar, G. D. & Hobbins, M. T. On the attribution of changing pan evaporation. *Geophys. Res. Lett.* **34**, 2007GL031166 (2007).
33. Chandrashekhar, V. India is a global warming "hole," and scientists aren't sure why. *Science* 388, 136 (2025).
34. Hodnebrog, Ø et al. Recent reductions in aerosol emissions have increased Earth's energy imbalance. *Commun. Earth Environ.* **5**, 166 (2024).
35. Priestley, C. H. B. & Taylor, R. J. On the assessment of surface heat flux and evaporation using large-scale parameters. *Mon. Weather Rev.* **100**, 81–92 (1972).
36. Sheffield, J., Wood, E. F. & Roderick, M. L. Little change in global drought over the past 60 years. *Nature* **491**, 435–438 (2012).
37. Fisher, J. B. et al. The future of evapotranspiration: global requirements for ecosystem functioning, carbon and climate feedbacks, agricultural management, and water resources. *Water Resour. Res.* **53**, 2618–2626 (2017).
38. Karimzadeh, S., Hartman, S., Chiarelli, D. D., Rulli, M. C. & D'Odorico, P. The tradeoff between water savings and salinization prevention in dryland irrigation. *Adv. Water Resour.* **183**, 104604 (2024).
39. Ghorbanpour, A. K., Peddinti, S. R., Hessels, T., Bastiaanssen, W. & Kisekka, I. Enhancing evapotranspiration estimates in composite terrain through the integration of satellite remote sensing and eddy covariance measurements. *Sci. Total Environ.* **963**, 178530 (2025).
40. Karimzadeh, S., Daccache, A., Rulli, M. C. & Ahamed, M. S. Global water-nutrient-salinity-energy nexus in lettuce production from open-field irrigation to closed-loop hydroponics in greenhouses. *J. Agric. Food Res.* 101935 https://doi.org/10.1016/j.jafr.2025.101935 (2025).
41. Ueyama, M. et al. Inferring CO_2 fertilization effect based on global monitoring land-atmosphere exchange with a theoretical model. *Environ. Res. Lett.* **15**, 084009 (2020).

42. Baldocchi, D., Chu, H. & Reichstein, M. Inter-annual variability of net and gross ecosystem carbon fluxes: a review. *Agric. For. Meteorol.* **249**, 520–533 (2018).

43. Muñoz-Sabater, J. et al. ERA5-land: a state-of-the-art global reanalysis dataset for land applications. *Earth Syst. Sci. Data* **13**, 4349–4383 (2021).

44. Xi, X., Zhuang, Q., Kim, S. & Gentine, P. Evaluating the effects of precipitation and evapotranspiration on soil moisture variability within CMIP5 using SMAP and ERA5 data. *Water Resour. Res.* **59**, e2022WR034225 (2023).

45. Ding, Y. & Peng, S. Spatiotemporal change and attribution of potential evapotranspiration over China from 1901 to 2100. *Theor. Appl. Climatol.* **145**, 79–94 (2021).

46. Scheff, J. & Frierson, D. M. W. Scaling potential evapotranspiration with greenhouse warming. *J. Clim.* **27**, 1539–1558 (2014).

47. Merino, R. A. & Gassmann, M. I. Trends of reference evapotranspiration and its physical drivers in southern South America. *Int. J. Climatol.* **43**, 1593–1609 (2023).

48. Tebakari, T., Yoshitani, J. & Suvanpimol, C. Time-space trend analysis in pan evaporation over Kingdom of Thailand. *J. Hydrol. Eng.* **10**, 205–215 (2005).

49. Puma, M. J. & Cook, B. I. Effects of irrigation on global climate during the 20th century. *J. Geophys. Res. Atmos.* **115**, D16120 (2010).

50. Boucher, O., Myhre, G. & Myhre, A. Direct human influence of irrigation on atmospheric water vapour and climate. *Clim. Dyn.* **22**, 597–603 (2004).

51. Javadian, M., Behrangi, A., Smith, W. K. & Fisher, J. B. Global trends in evapotranspiration dominated by increases across large cropland regions. *Remote Sens.* **12**, 1221 (2020).

52. Matsoukas, C. et al. Potential evaporation trends over land between 1983–2008: driven by radiative fluxes or vapour-pressure deficit? *Atmos. Chem. Phys.* **11**, 7601–7616 (2011).

53. Ahmadi, A., Kazemi, M. H., Daccache, A. & Snyder, R. L. SolarET: a generalizable machine learning approach to estimate reference evapotranspiration from solar radiation. *Agric. Water Manag.* **295**, 108779 (2024).

54. Byrne, M. P. & O'Gorman, P. A. Trends in continental temperature and humidity directly linked to ocean warming. *Proc. Natl. Acad. Sci. USA* **115**, 4863–4868 (2018).

55. Kim, Y. & Johnson, M. S. Deciphering the role of evapotranspiration in declining relative humidity trends over land. *Commun. Earth Environ.* **6**, 105 (2025).

56. Ambika, A. K. & Mishra, V. Substantial decline in atmospheric aridity due to irrigation in India. *Environ. Res. Lett.* **15**, 124060 (2020).

57. Wu, L., Feng, J., Qin, F. & Qiu, Y. Regional climate effects of irrigation over Central Asia using Weather Research and Forecasting model. *JGR Atmos.* **127**, e2021JD036210 (2022).

58. Mehta, P. et al. Half of twenty-first century global irrigation expansion has been in water-stressed regions. *Nat. Water* **2**, 254–261 (2024).

59. Song, S., Zhang, X. & Liu, J. Effects of irrigation-induced surface thermodynamics changes on wind speed in the Heihe river basin, Northwest China. *Int. J. Climatol.* **44**, 3445–3463 (2024).

60. De Kok, R. J., Tuinenburg, O. A., Bonekamp, P. N. J. & Immerzeel, W. W. Irrigation as a potential driver for anomalous glacier behavior in high mountain Asia. *Geophys. Res. Lett.* **45**, 2047–2054 (2018).

61. Lu, J. et al. A harmonized global land evaporation dataset from model-based products covering 1980–2017. *Earth Syst. Sci. Data* **13**, 5879–5898 (2021).

62. Zhang, K. et al. Vegetation greening and climate change promote multidecadal rises of global land evapotranspiration. *Sci. Rep.* **5**, 15956 (2015).

63. Zhang, Y. et al. Multi-decadal trends in global terrestrial evapotranspiration and its components. *Sci. Rep.* **6**, 19124 (2016).

64. Yang, Y. et al. Evapotranspiration on a greening Earth. *Nat. Rev. Earth Environ.* **4**, 626–641 (2023).

65. Baldocchi, D. D., Keeney, N., Rey-Sanchez, C. & Fisher, J. B. Atmospheric humidity deficits tell us how soil moisture deficits down-regulate ecosystem evaporation. *Adv. Water Resour.* **159**, 104100 (2022).

66. Siebert, S. et al. A global data set of the extent of irrigated land from 1900 to 2005. *Hydrol. Earth Syst. Sci.* **19**, 1521–1545 (2015).

67. Siebert, S. & Döll, P. Quantifying blue and green virtual water contents in global crop production as well as potential production losses without irrigation. *J. Hydrol.* **384**, 198–217 (2010).

68. Van Der Ent, R. J., Savenije, H. H. G., Schaefli, B. & Steele-Dunne, S. C. Origin and fate of atmospheric moisture over continents. *Water Resour. Res.* **46**, WR009127 (2010).

69. Vicente-Serrano, S. M. et al. Recent changes of relative humidity: regional connections with land and ocean processes. *Earth Syst. Dynam.* **9**, 915–937 (2018).

70. Latif, M. et al. Strengthening atmospheric circulation and trade winds slowed tropical Pacific surface warming. *Commun. Earth Environ.* **4**, 249 (2023).

71. Bandara, J. S. & Cai, Y. The impact of climate change on food crop productivity, food prices and food security in South Asia. *Econ. Anal. Policy* **44**, 451–465 (2014).

72. Rehman, A., Batool, Z., Ma, H., Alvarado, R. & Oláh, J. Climate change and food security in South Asia: the importance of renewable energy and agricultural credit. *Humanit Soc. Sci. Commun.* **11**, 342 (2024).

73. Baig, F. et al. Synergies and struggles: water security and climate action in South Asia's quest for SDG 6 and SDG 13. *Gondwana Res.* **148**, 393–414 (2025).

74. Copernicus Climate Change Service. Agrometeorological indicators from 1979 up to 2019 derived from reanalysis. ECMWF https://doi.org/10.24381/CDS.6C68C9BB (2019).

75. Copernicus Climate Change Service. ERA5-Land hourly data from 1950 to present. Copernicus Climate Change Service (C3S) Climate Data Store (CDS) https://doi.org/10.24381/CDS.E2161BAC (2019).

76. Zhou, C. & Wang, K. Evaluation of surface fluxes in ERA-interim using flux tower data. *J. Clim.* **29**, 1573–1582 (2016).

77. Martens, B. et al. Evaluating the land-surface energy partitioning in ERA5. *Geosci. Model Dev.* **13**, 4159–4181 (2020).

78. Baldocchi, D. et al. FLUXNET: a new tool to study the temporal and spatial variability of ecosystem–scale carbon dioxide, water vapor, and energy flux densities. *Bull. Am. Meteorol. Soc.* **82**, 2415–2434 (2001).

79. Danielson, J. J. & Gesch, D. B. *Global Multi-Resolution Terrain Elevation Data 2010 (GMTED2010)* https://pubs.usgs.gov/publication/ofr20111073, https://doi.org/10.3133/ofr20111073 (USGS, 2011).

80. Parker, W. S. Reanalyses and observations: what's the difference? *Bull. Am. Meteorol. Soc.* **97**, 1565–1572 (2016).

81. Lavers, D. A., Simmons, A., Vamborg, F. & Rodwell, M. J. An evaluation of ERA5 precipitation for climate monitoring. *Quart. J. R. Meteor. Soc.* **148**, 3152–3165 (2022).

82. Harris, I., Osborn, T. J., Jones, P. & Lister, D. Version 4 of the CRU TS monthly high-resolution gridded multivariate climate dataset. *Sci. Data* **7**, 109 (2020).

83. Kendall, M. G. A new measure of rank correlation. *Biometrika* **30**, 81 (1938).

84. Mann, H. B. Nonparametric tests against trend. *Econometrica* **13**, 245 (1945).

85. Hu, Z., Liu, S., Zhong, G., Lin, H. & Zhou, Z. Modified Mann-Kendall trend test for hydrological time series under the scaling hypothesis and its application. *Hydrol. Sci. J.* **65**, 2419–2438 (2020).

86. Karimzadeh, S., Ahmadi, A., Baldocchi, D. & Fisher, J. Global trends in hydroclimatic variables (1979–2023) from ERA5 at 0.25° resolution. Preprint at https://doi.org/10.5281/ZENODO.17098484 (2025).

Author contributions

S.K. and A.A. conceived and designed the study, with A.A. and J.B.F. providing significant intellectual guidance and D.B. contributing conceptual insights. S.K. conducted the data analysis using the Copernicus Climate Data Store and performed the spatial analysis. S.K. and A.A. drafted the initial manuscript, incorporating feedback and revisions from all co-authors.

Competing interests

The authors declare no competing interests.

Additional information

Supplementary information The online version contains supplementary material available at https://doi.org/10.1038/s43247-025-02959-x.

Correspondence and requests for materials should be addressed to Saeed Karimzadeh or Arman Ahmadi.

Peer review information *Communications Earth & Environment* thanks Christian Massari and the other anonymous reviewer(s) for their contribution to the peer review of this work. Primary handling editor: Nicola Colombo. A peer review file is available.

Reprints and permissions information is available at http://www.nature.com/reprints

Publisher's note Springer Nature remains neutral with regard to jurisdictional claims in published maps and institutional affiliations.